Anisotropic physical properties and large critical current density in $KCa_2Fe_4As_4F_2$ single crystal

Sunseng Pyon,[1] Yuto Kobayashi,[1] Ayumu Takahashi,[1] Wenjie Li,[1] Teng Wang,[2] Gang Mu,[2] Ataru Ichinose,[3] Tadashi Kambara,[4] Atsushi Yoshida,[4] and Tsuyoshi Tamegai[1]

[1]*Department of Applied Physics, The University of Tokyo, 7-3-1 Hongo, Bunkyo-ku, Tokyo 113–8656, Japan*

[2]*State Key Laboratory of Functional Materials for Informatics, Shanghai Institute of Microsystem and Information Technology, Chinese Academy of Sciences, Shanghai 200050, China*

[3]*Central Research Institute of Electric Power Industry, Electric Power Engineering Research Laboratory, 2-6-1, Nagasaka, Yokosuka-shi, Kanagawa 240–0196, Japan*

[4]*Nishina Center, RIKEN, 2-1 Hirosawa, Wako, Saitama 351–0198, Japan*

(Received 8 June 2020; accepted 30 September 2020; published 21 October 2020)

We present a systematic study of electrical resistivity, Hall coefficient, magneto-optical imaging, magnetization, and scanning transmission electron microscopy (STEM) analyses of $KCa_2Fe_4As_4F_2$ single crystals. Sharp diamagnetic transition and magneto-optical imaging reveal homogeneity of single crystal and prominent Bean-like penetrations of vortices. Large anisotropy of electrical resistivity, with $\rho_c/\rho_{ab} > 100$, and semiconductorlike ρ_c suggest that the electronic state is quasi-two-dimensional. Hall effect measurements indicate that $KCa_2Fe_4As_4F_2$ is a multiband system with holes as main carriers. Magnetization measurements reveal significantly larger J_c compared with that in other iron-based superconductors with different values of J_c depending on the direction of magnetic field. The origin of these J_c characteristics is discussed based on microstructural observations using STEM. In addition, further enhancement of J_c in $KCa_2Fe_4As_4F_2$ for future high-field application is demonstrated in terms of heavy-ion irradiation.

DOI: 10.1103/PhysRevMaterials.4.104801

I. INTRODUCTION

The discovery of iron-based superconductors (IBSs) in 2008 [1] has prompted great interest in the field of condensed matter physics. Their multigap superconductivity due to their multiband electronic structures were studied. Not only their unconventional superconducting mechanism leading to high transition temperature, but also their potential for applications has been extensively studied and several types of IBSs are expected as candidates for future high-field applications [2–4]. In the case of widely studied IBSs such as the 122-type $(Ba,K)Fe_2As_2$ [5], their electronic states are three-dimensional with weak anisotropy. It makes a good contrast to two-dimensional electronic states in cuprate superconductors. Recently, however, it is suggested that quasi-two-dimensional electronic states emerge in IBSs such as 12442-type compounds [6–10] or some IBSs consisting of FeSe layers sandwiched by thick insulating layers [11,12]. The 12442-type IBSs, a series of bilayered compounds $AB_2Fe_4As_4C_2$ (A = K, Rb, and Cs; B = Ca, Nd, Sm, Gd, Tb, Dy, and Ho; and C = F and O) are recognized as the intergrowth of 1111- and 122-type IBSs, and are reported to be superconductors with superconducting transition temperature $T_c = 28-37$ K [6–10]. The 12442-type IBSs have double Fe_2As_2 conducting layers between two neighboring Ca_2F_2 insulating layers [6]. Based on the first-principles calculation, 10 bands crossing the Fermi level are predicted, which are more complicated than other IBSs, showing multiband character [13]. Using polycrystalline samples of 12442-type IBSs, their electronic and magnetic structures have been investigated [14–16]. Furthermore, very recently, the growth of millimeter-sized high-quality single crystals of 12442-type IBSs was reported [17,18]. It is needless to say that studies on high-quality single crystals are essential to reveal intrinsic properties of these superconductors. Using these single crystals, electronic states with large anisotropy were revealed by the estimation of the upper critical field, H_{c2} [17,18], and torque analyses [19]. In addition, neutron spin resonance measurements revealed quasi-two-dimensional electronic behavior of $KCa_2Fe_4As_4F_2$, which is similar to those of highly anisotropic cuprate superconductors [20]. Not only elucidation of unconventional superconductivity, but also the possibility of future high-field application of this material are intriguing topics. H_{c2} of $KCa_2Fe_4As_4F_2$ is much larger than that of other systems of IBSs, when the magnetic field is applied along the ab plane, and large anisotropy parameter $\gamma (=H_{c2}^{ab}/H_{c2}^{c}) \sim 8$ was revealed near the superconducting transition [17,21,22]. Large H_{c2} is helpful for future high-field applications. Although critical current density, J_c, in $KCa_2Fe_4As_4F_2$ has not been reported yet, a recent report on J_c in $CsCa_2Fe_4As_4F_2$ at 2 K under self-field is comparable to that in well-studied 122-type materials [18,23]. In general, isotropic superconductors are favored in high-field and high-current applications. Recently, however, coated conductors of $REBa_2Cu_3O_7$ (RE: Rare Earth), with $\gamma \sim 7$, and multifilamentary tapes of $(Bi,Pb)_2Sr_2Ca_2Cu_3O_x$, with $\gamma \sim 100$, have been developed, and are commercially available [24]. These facts demonstrate that anisotropic superconductors like 12442-type compounds can be used for superconducting wires or tapes for high-magnetic applications by adding artificial pinning centers or

implementing local grain alignment to superconducting cores. Further studies on J_c in 12442-type IBSs are needed.

In this paper, we characterize the superconducting properties of $KCa_2Fe_4As_4F_2$ single crystals by measuring anisotropic electrical resistivity, in-plane Hall coefficient, and anisotropic irreversible magnetization. The quality and microstructure of single crystals were also characterized by magneto-optical imaging and scanning transmission electron microscopy (STEM). The electronic structure of $KCa_2Fe_4As_4F_2$ is discussed by comparing it with that in other IBSs. In addition, we found significantly large in-plane J_c in $KCa_2Fe_4As_4F_2$ compared with that in other IBSs, and unique anisotropy of J_c depending on the direction of magnetic field. Further enhancement of J_c in $KCa_2Fe_4As_4F_2$ for future high-field application in terms of heavy-ion irradiation is also demonstrated.

II. EXPERIMENTAL METHODS

Single crystals of $KCa_2Fe_4As_4F_2$ were grown using the self-flux method with KAs as flux. Details of sample growth and basic physical properties have been reported in Ref. [17]. Electrical resistivity along the *ab* plane (ρ_{ab}) and along the *c* axis (ρ_c) were measured by the four-probe method. Anticipating relatively large anisotropy of transport properties based on the previous measurements [17], electrical contacts were prepared to pass the current uniformly as discussed later. In the case of ρ_{ab} measurement, consistency of the values evaluated on the top and bottom surfaces was examined. The Hall voltage was measured with a Quantum Design physical property measurement system with the AC transport option with current density of $\sim$11 A/cm^2. The Hall voltage was obtained from the antisymmetric part of transverse voltage by subtracting the positive and negative magnetic field data. Macroscopic homogeneity of superconductivity was examined by measuring the critical state field profile using magneto-optical (MO) imaging. For MO imaging, an iron-garnet indicator film was placed in direct contact with the sample surface, and the whole assembly was attached to the cold finger of a He-flow cryostat (Microstat-HR, Oxford Instruments). MO images were acquired by using a cooled-CCD camera with 12-bit resolution (ORCA-ER, Hamamatsu). Cross-sectional observations of the single crystals were performed with a STEM (JEOL, JEM-2100F). The spatial resolution of JEOL JEM-2100F microscope is 0.2 nm. However, we set it as 0.5 nm to add contrast in the STEM image. The specimen for STEM were prepared by digging and milling using a focused-ion beam (FIB), which is called the microsampling technique. The final milling using FIB was conducted at an acceleration voltage of 30 kV and with a very weak ion current of $\sim$10 pA without tilting the specimen. Enhancement of J_c was attempted by irradiating 2.6 GeV U ion along the *c* axis at RIKEN Ring Cyclotron in RI Beam Factory operated by RIKEN Nishina Center and CNS, The University of Tokyo. The irradiation dose is evaluated by the dose-equivalent magnetic field called "matching field", at which all defects are occupied by single vortices, $B_\Phi = n\Phi_0$. Here, n is the areal density of CDs and Φ_0 is a flux quantum. Columnar defects at a dose-equivalent matching fields of $B_\Phi = 40$ kG were created. U-ion beam was directly irradiated to the crystal without any shielding or foils.

TABLE I. Dimensions of $KCa_2Fe_4As_4F_2$ single crystals.

No.	Dimensions(μm^3)	Measurements	Related figures
1	510 × 390 × 7.8	Magnetization (to determine T_c and J_c for pristine sample)	Figs. 1, 7, 9
2	316 × 196 × 9.1	MO	Fig. 2
3	920 × 392 × 8.0	ρ_{ab}	Figs. 3, 4, 5
4	878 × 236 × 3.0	ρ_{ab}	Fig. 3
5	520 × 326 × 13.0	ρ_c	Fig. 5
6	784 × 730 × 12.0	R_H	Fig. 6
7	263 × 228 × 11.1	Magnetization (to determine J_c for U-irradiate sample)	Fig. 8

Information of crystals for measurements is summarized in Table I.

III. RESULTS AND DISCUSSIONS

A. Characterization of $KCa_2Fe_4As_4F_2$ crystal

Figure 1 shows the temperature dependence of magnetization ($H \parallel c$ axis) at 5 Oe for sample No. 1. T_c defined by the onset of diamagnetism is 33.0 K and ΔT_c is less than 1 K. The quality of the sample is almost the same as that reported in the previous publication [17].

MO imaging of sample No. 2 was performed to evaluate its homogeneity and quality. Figures 2(a) and 2(b) display MO images of $KCa_2Fe_4As_4F_2$ in the remanent state at (a) 5 K and (b) 20 K, respectively, after cycling the field up to 1.2 kOe for 0.2 s. The crystal for MO measurements are cut into a parallelepiped with smooth surface and no visible cracks as shown in the optical micrograph of Fig. 2(c). At 5 K, the magnetic field is mostly shielded and only partially penetrates the sample due to large J_c and the limitation of the value of the applied field. A faint horizontal white line near the center of the crystal may indicate a small crack which is invisible from the surface. At 20 K, the magnetic field reaches the center

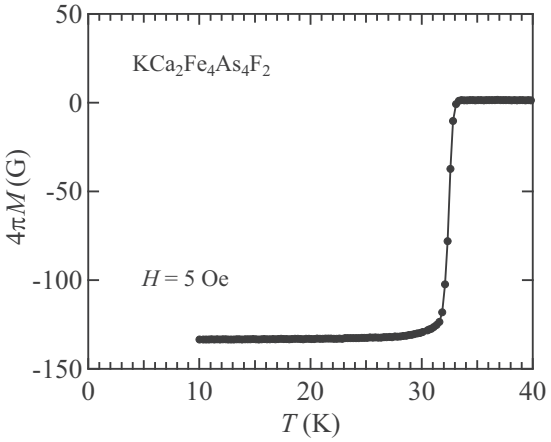

FIG. 1. Temperature dependence of the zero-field-cooled magnetization at $H = 5$ Oe along the *c* axis in $KCa_2Fe_4As_4F_2$.

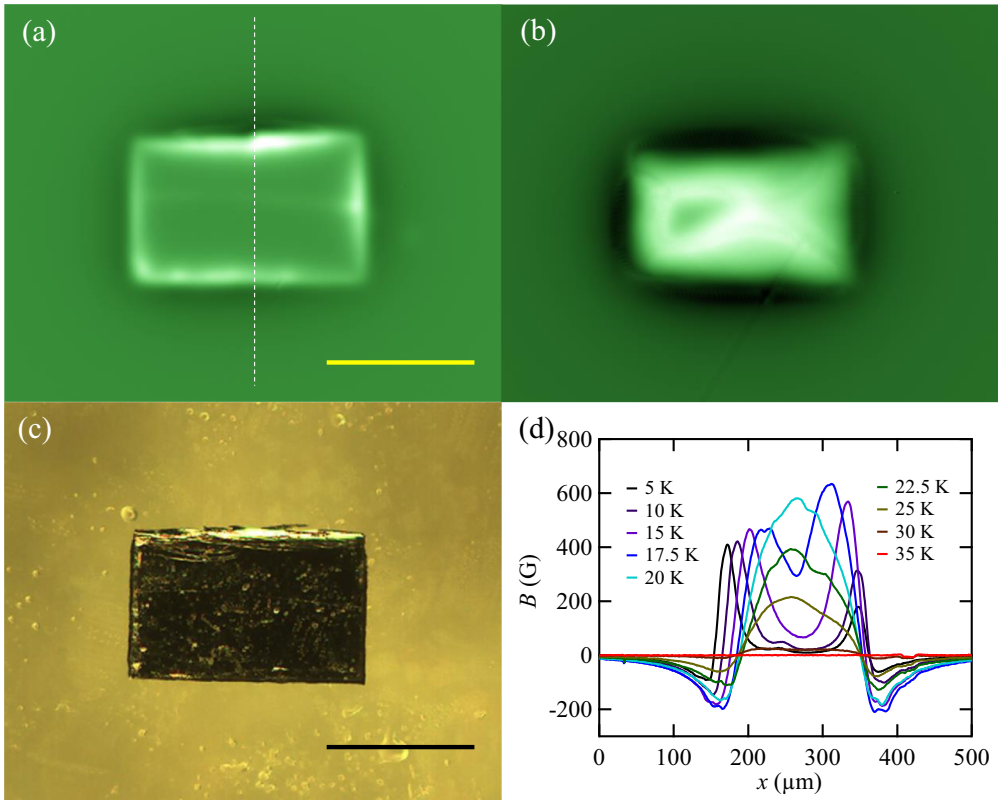

FIG. 2. Differential MO images of $KCa_2Fe_4As_4F_2$ in the remanent state at (a) 5 K and (b) 20 K after cycling the field up to 1.6 kOe for 0.2 s. (c) An optical micrograph of $KCa_2Fe_4As_4F_2$. (d) Local magnetic induction profiles at different temperatures taken along the dashed line in (a). Both the yellow bar in (a) and black bar in (c) correspond to 200 μm.

of the sample and the MO image of the right part shows the critical state field profile expected for a uniform thin-plate superconductor with clear current-discontinuity lines (d lines), although the magnetic field in the left half of the sample is not fully penetrated. These results indicate that the sample is fairly homogeneous with a weak variation of J_c in the crystal. Local magnetic induction profiles at different temperatures taken along the dashed line in Fig. 2(a) are shown in Fig. 2(d). Magnetic induction profiles at higher temperatures of 20 $\sim$ 30 K show rooftop patterns, indicating that the large and homogeneous current flows throughout the sample. From the value of the trapped field, J_c can be roughly evaluated [25]. At 20 K, trapped magnetic induction ΔB is 581 G. Using the approximate formula between ΔB and J_c for a thin superconductor with a thickness t, $J_c \sim \Delta B/(t * \beta)$, with $t = 9.1\ \mu$m (β is a parameter determined by the sample dimensions and the distance between the sample surface and the garnet film, and $\beta \sim 3.3$ in the present case) [25], J_c at 20 K under the self-field is evaluated as 0.19 MA/cm^2.

B. Electrical properties (ρ_{ab}, ρ_c, and R_H)

The superconducting transition and electrical characteristics are also evaluated by the temperature dependence of ρ_{ab}. Two kinds of samples, No. 3 and No. 4 as shown in Table I with different contact configurations are measured. The contact configuration for samples No. 3 and No. 4 are shown in Fig. 3(a). Temperature dependences of ρ_{ab} of the two samples are shown in Fig 3(b). The absolute value of $\rho_{ab} \sim 300\ \mu\Omega$ cm at room temperature and their temperature dependences are consistent with each other. Both samples show sharp superconducting transitions at $\sim$34.0 K. When the electrical resistivity of anisotropic crystals is evaluated, it is possible that the resistivity is estimated incorrectly due to inhomogeneous current flow, in particular along the direction perpendicular to the surface. However, the fact that ρ_{ab} of sample No. 4, where voltage contacts are attached on the opposite surface to the current contacts agrees with that of sample No. 3 with all contacts on the same surface, suggest that we can ignore the possible error in the absolute value of ρ_{ab} due to sample inhomogeneity and anisotropy. As shown in Fig. 3(b), $\rho_{ab}(T)$ shows a tendency of saturation with increasing temperature. Similar saturating behaviors are also observed such as in K-doped $BaFe_2As_2$ [26], or $CaKFe_4As_4$ [27,28], and values of ρ_{ab} at room temperature are very similar. In general, an electrical resistivity is inversely proportional to the mean free path of electrons l in metals. As Ioffe and Regel argued, metallic conduction occurs only when l is larger than the interatomic spacing a [29]. So maximum resistivity is limited, and that is maximized when l is comparable to a. This limit known as Mott-Ioffe-Regel (MIR) limit, universally observed in several metals, and the values of saturated resistivity around 100–400 $\mu\Omega$ cm were reported [30]. By considering the similarity of $\rho_{ab}(T)$ and lattice parameter between $KCa_2Fe_4As_4F_2$ and K-doped $BaFe_2As_2$ or $CaKFe_4As_4$, $\rho_{ab} \sim 300\ \mu\Omega$ cm at room temperature is more plausible than that $\sim$1.3 mΩ cm in a previous report [17]. We tried to estimate the residual resistivity at 0 K, ρ(0 K),

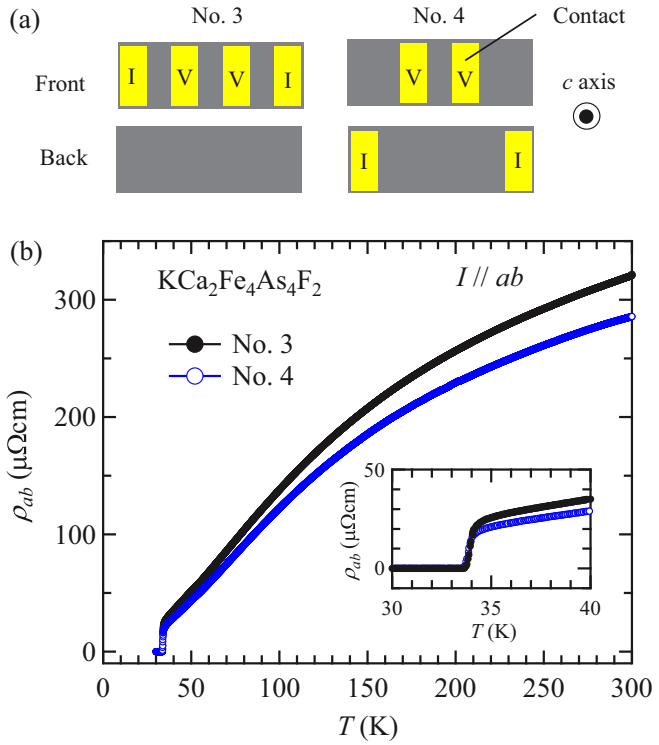

FIG. 3. (a) Schematic drawings of the two samples with electrical contacts for measurements of in-plane electrical resistivity (ρ_{ab}). (b) Temperature dependence of ρ_{ab} in $KCa_2Fe_4As_4F_2$ samples No. 3 and No. 4 measured in a temperature range of 30–300 K. The inset in (b) shows $\rho_{ab} - T$ near T_c.

by curve fitting using the equation $\rho(T) = \rho(0\,\mathrm{K}) + A_1T + A_2T^2$ and $\rho(T) = \rho(0\,\mathrm{K}) + AT^n$, over the range of 40 to 80 K to evaluate the sample quality. We observed negative $\rho(0\,\mathrm{K})$ values obtained by these two fittings due to the relatively large T-linear contribution in this temperature range. Similar negative $\rho(0\,\mathrm{K})$ was also observed in $Ba_{1-x}K_xFe_2As_2$ [31]. The obtained exponent of $n \sim 1.3$ for $KCa_2Fe_4AsF_2$ is a little bit smaller than that of $n \sim 1.4$–2.0 in $Ba_{1-x}K_xFe_2As_2$, which suggests a larger T-linear contribution. Instead of the extrapolated $\rho(0\,\mathrm{K})$, the sample quality was evaluated by the resistivity value just above T_c, $\rho(36\,\mathrm{K})$, which is 28.2 and 23.1 $\mu\Omega$ cm for samples No. 3 and No. 4, respectively. With these values of $\rho(36\,\mathrm{K})$, the residual resistivity ratio (RRR) is defined by $\rho(300\ \mathrm{K})/\rho(36\,\mathrm{K})$, resulting in RRR $\sim$ 11.4 or 12.3, respectively. In a similar compound of $CaKFe_4As_4$, RRR [$\rho(300\ \mathrm{K})/\rho(35\ \mathrm{K})$] of $\sim$15 has been reported [27]. Relatively large RRR, small residual resistivity, and sharp transition width indicate that our crystals are of high quality.

Figures 4(a) and 4(b) show the temperature dependence of ρ_{ab} of sample No. 3 for the $H \parallel c$ axis and $H \parallel ab$ plane measured at various magnetic fields up to 50 kOe. As the magnetic field is increased, the superconducting transition for the $H \parallel c$ axis broadens compared with that for the $H \parallel ab$ plane. Two kinds of irreversibility fields, for fields along the c axis (H_{irr}^{c}) or ab plane (H_{irr}^{ab}), were also estimated from ρ_{ab} data. They are defined by the criteria of $\rho_{ab} \sim 0.5\,\mu\Omega\,\mathrm{cm}$. Obtained temperature dependences of H_{irr}^{c} and H_{irr}^{ab} are shown in Fig. 4(c). We also evaluate two kinds of H_{c2}, for

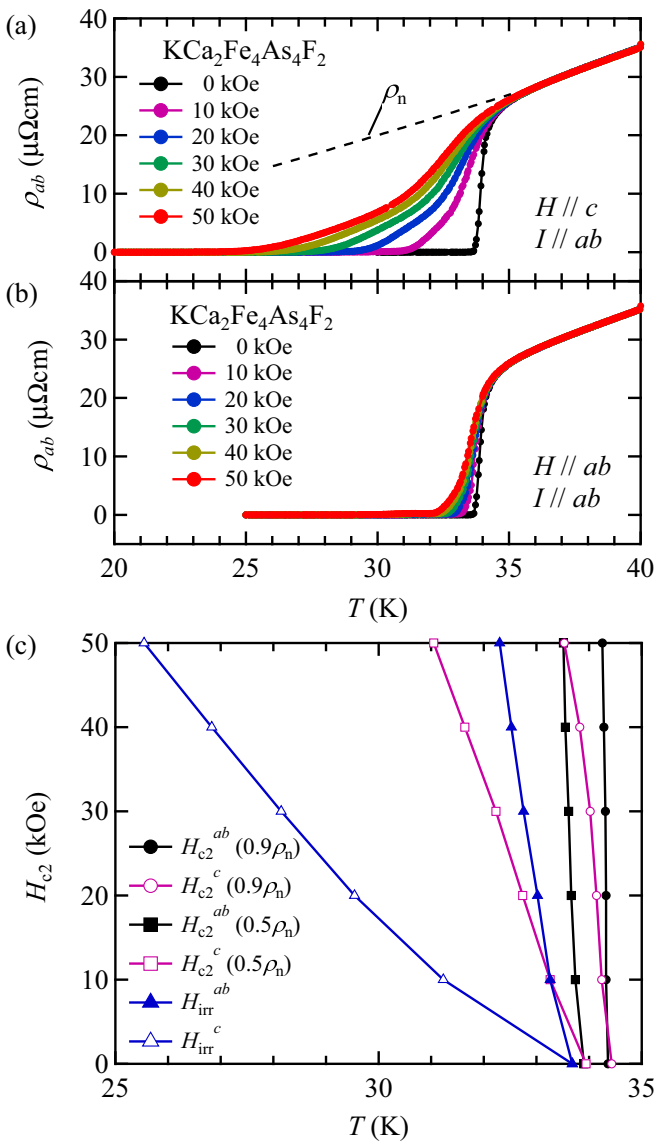

FIG. 4. Temperature dependence of in-plane electrical resistivity (ρ_{ab}) in $KCa_2Fe_4As_4F_2$ (No. 3) below 40 K under various magnetic fields parallel to the (a) c axis and (b) ab plane. (c) Anisotropic H_{c2} and H_{irr} evaluated from temperature-dependent resistivity in (a) and (b). H_{c2} is defined by two different criteria of $0.9\rho_n$ and $0.5\rho_n$. Here, ρ_n is the normal state resistivity estimated from the extrapolation of the resistivity using the power-law form with $n = 1.3$ as shown in the dashed line in (a). H_{irr} is defined by the criteria of $\rho_{ab} \sim 0.5\,\mu\Omega\,\mathrm{cm}$.

fields along c axis (H_{c2}^{c}) or ab plane (H_{c2}^{ab}), by applying the Wethamer-Helfand-Hohenberg formula, $H_{c2}(0\,\mathrm{K}) = -0.693T_c\mathrm{d}H_{c2}/\mathrm{d}T(T = T_c)$ [32], and obtained $H_{c2}(T)$ as shown in Fig. 4(c). H_{c2} is defined by the two different criteria of $0.9\rho_n$ and $0.5\rho_n$. Here, ρ_n is the normal state resistivity estimated from the extrapolation of the resistivity using the power-law form with $n = 1.3$ as shown in the dashed line in Fig. 4(a). The estimated H_{c2}^{ab} (0 K) is 10 820 and 3012 kOe, and $H_{c2}^{c}(0\,\mathrm{K})$ is 1326 and 407 kOe, for $0.9\rho_n$ and $0.5\rho_n$, respectively. Using these data, the anisotropy parameter $\gamma = H_{c2}^{ab}/H_{c2}^{c}$ is also evaluated as 8.2 and 7.4 for $0.9\rho_n$ and $0.5\rho_n$, respectively. These estimated values of γ

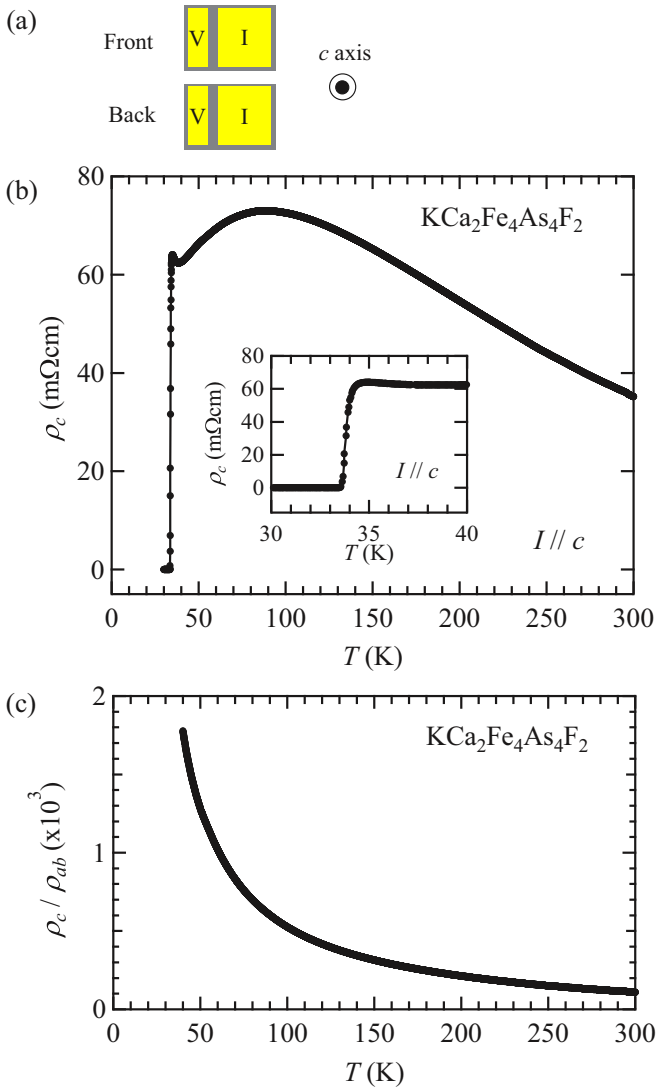

FIG. 5. (a) Schematic drawings of the electrical contacts for the measurement of out-of-plane electrical resistivity (ρ_c). (b) Temperature dependence of ρ_c in $KCa_2Fe_4As_4F_2$ in a temperature range of 30–300 K under zero magnetic field. The inset in (b) shows ρ_c-T near T_c. (c) Temperature dependence of the anisotropy of the resistivity, ρ_c/ρ_{ab}. ρ_{ab} of sample No. 3 shown in Fig. 3(b) is used for the calculation.

and $H_{c2}^{ab}(0\ \mathrm{K})$ are similar to that in the previous report [17], and larger than those of other IBSs [27,33–35].

To discuss the anisotropy of $KCa_2Fe_4As_4F_2$, we measured ρ_c for sample No. 5. A schematic drawing of the electrical contacts attached to $KCa_2Fe_4As_4F_2$ for ρ_c measurements is shown in Fig. 5(a). Compared with ρ_{ab}, the magnitude and temperature dependence of ρ_c are very different. As shown in Fig. 5(b), the ρ_c at room temperature is 35 mΩ cm, which is almost 100 times larger than the value of ρ_{ab} shown in Fig. 3(b). In the simplest scenario, the anisotropy of the resistivity should be equal to γ^2. ρ_c/ρ_{ab} using the ρ_{ab} of sample No. 3 is shown in Fig. 5(c). ρ_c/ρ_{ab} at room temperature is ∼100, which is close to γ^2 evaluated from the anisotropy of H_{c2}. ρ_c/ρ_{ab} increases with decreasing temperature, reaching a very large value of ∼1800 around T_c. These values are larger than that in doped and nondoped $BaFe_2As_2$ (∼100 [35] or ∼4 [36,37]). The value of ρ_c/ρ_{ab} larger than 100 with increasing trend with decreasing temperature are also observed in cuprate superconductors [38–40] and some IBS compounds such as $(Li_{0.84}Fe_{0.16})OHFe_{0.98}Se$ [11] and $Li_x(NH_3)_yFe_2Se_2$ [12], where highly two-dimensional electronic states are suggested. In $La_{2-x}Sr_xCuO_4$, ρ_c/ρ_{ab} overdoped with $x \sim 0.3$, where Fermi-liquid-like metallic resistivity ($\rho \sim T^\alpha$, $\alpha > 1$) is observed, is almost temperature independent. On the other hand, that underdoped with $x < 0.2$ increases with decreasing temperature [38], which is similar to that in $KCa_2Fe_4As_4F_2$. These results can be understood by the quasi-two-dimensional Fermi-surface sheets revealed by the first-principles calculations [8,9,13]. Furthermore, temperature dependence of ρ_c shows a broad maximum with its maximum at around 90 K, and a tiny kink just above T_c. Similar behavior is reported in $CsCa_2Fe_4As_4F_2$ single crystal [18]. A broad maximum in ρ_c-T has also been observed in the same 12442-type of $CsCa_2Fe_4As_4F_2$ [18], or $(Li_{0.84}Fe_{0.16})OHFe_{0.98}Se$ [11], and $Li_x(NH_3)_yFe_2Se_2$ [12]. This crossover of temperature dependence of ρ_c may suggest an opening of pseudogap in $KCa_2Fe_4As_4F_2$ as suggested by Refs. [41–43].

The Hall resistivity ρ_{yx} for sample No. 6 as a function of magnetic field up to 50 kOe at several temperatures are shown in Fig. 6(a). In the whole range, ρ_{yx} is positive and shows linear field dependence up to 50 kOe. The Hall coefficient R_H in $KCa_2Fe_4As_4F_2$ obtained from ρ_{yx} is plotted in Fig. 6(b). The sign of R_H is positive in the whole temperature range, which is consistent with the self-hole-doping scenario based on the first-principles calculation [13]. R_H increases with decreasing temperature from 300 to 80 K, and stays nearly constant below 80 K. The absolute value of R_H around T_c is two times larger than that at 300 K. The absolute value of R_H in our single crystal is smaller than that of R_H in the polycrystalline sample [6,14]. Around 75 K where R_H takes its maximum value, R_H of the single crystal and polycrystalline sample are ∼1.5 and $2.0 \times 10^{-3}\ \mathrm{cm^3/C}$, respectively. The larger R_H in the polycrystalline sample could be originated from the increase of Hall resistivity caused by lower packing density and the anisotropy of the Hall coefficient. The absolute value of R_H at 300 K, $\sim 0.7 \times 10^{-3}\ \mathrm{cm^3/C}$, is similar to that of other IBSs such as $Ba(Fe_{1-x}Co_x)_2As_2$ ($\sim 1.1 \times 10^{-3}\ \mathrm{cm^3/C}$ for $x = 0.1$) [44], $Ba_{1-x}K_xFe_2As_2$ ($\sim 0.5 \times 10^{-3}\ \mathrm{cm^3/C}$ for $x \sim 0.5$) [45] or $CaKFe_4As_4$ ($\sim 0.4 \times 10^{-3}\ \mathrm{cm^3/C}$) [27]. It is noteworthy that doped carriers to FeAs layer in $KCa_2Fe_4As_4F_2$ should be almost the same as those in $Ba_{0.5}K_{0.5}Fe_2As_2$ and $CaKFe_4As_4$, since the number of doped hole per Fe is the same in these three compounds. Similar values of R_H in these compounds are consistent with the simple hole-doping scenario. The temperature dependence of R_H shown in Fig. 6(b) is consistent with a multiband electronic structure of $KCa_2Fe_4As_4F_2$. In a simple single-band system, the Hall coefficient is given by $R_H = 1/nqc$, where q is the charge of a carrier, n is the carrier density, c is the speed of light, and R_H is T independent. By contrast, the Hall coefficient in a multiband system, for instance, consisting of electron and hole bands, is given by $R_H = (n_h\mu_h^2 - n_e\mu_e^2)/[e(n_h\mu_h + n_e\mu_e)^2]$, where n_h (n_e) is the density of holes (electrons) and μ_h (μ_e) is the mobility of holes (electrons). The obtained results indicate

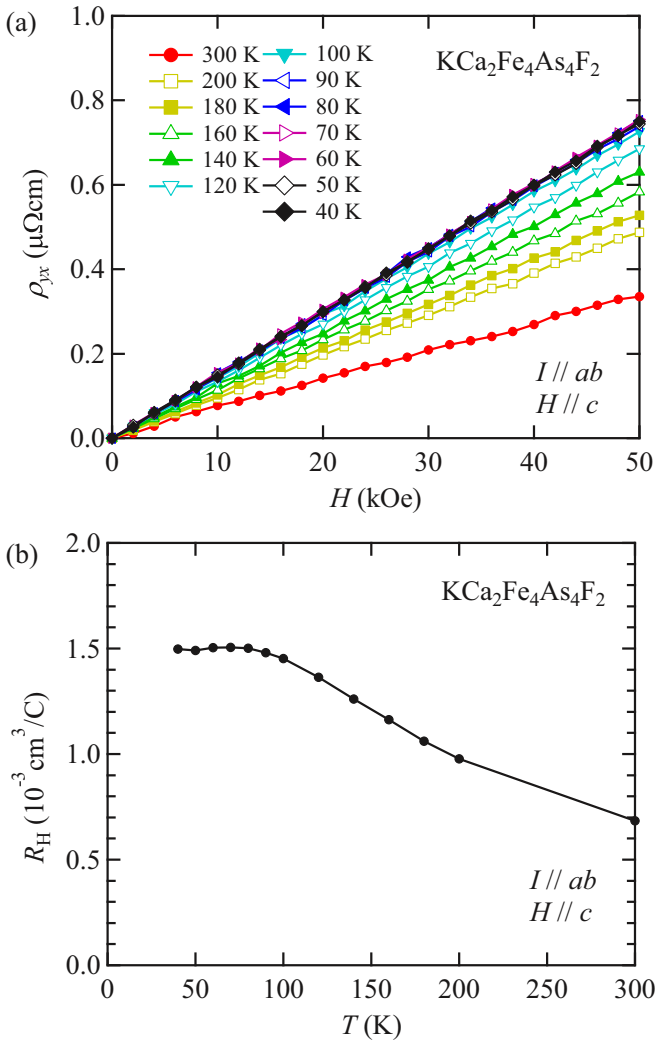

FIG. 6. (a) Hall resistivity ρ_{yx} as a function of field at various temperatures in $KCa_2Fe_4As_4F_2$. (b) Temperature dependence of the Hall coefficient R_H in $KCa_2Fe_4As_4F_2$.

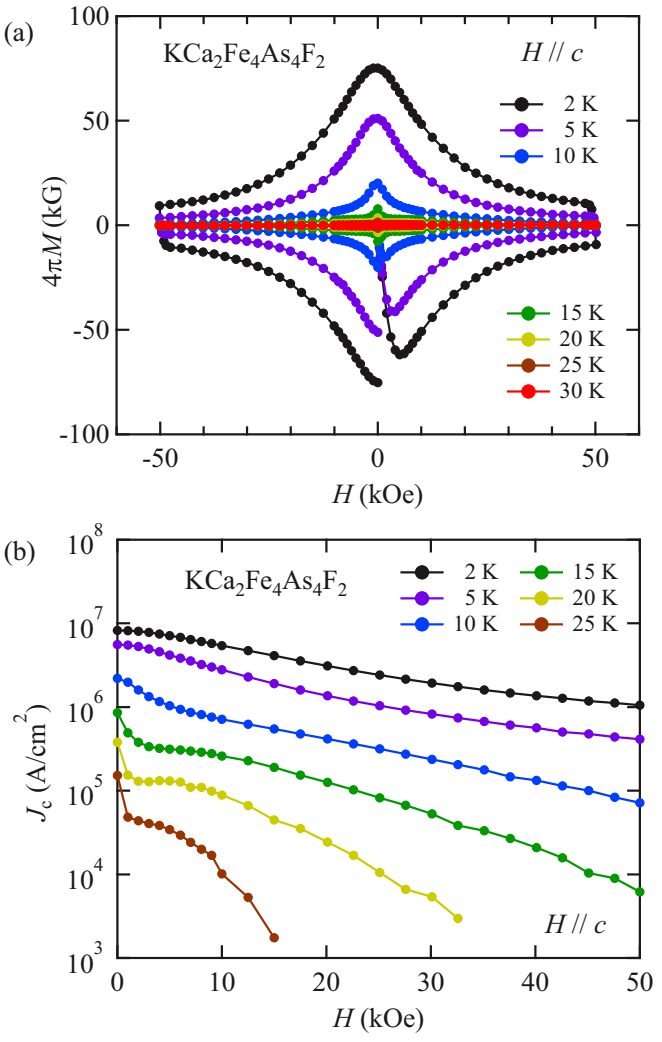

FIG. 7. (a) Magnetic field dependence of magnetization in $KCa_2Fe_4As_4F_2$ at various temperatures for $H \parallel c$ axis. (b) Magnetic field dependence of in-plane J_c evaluated using the data shown in (a).

that $KCa_2Fe_4As_4F_2$ is a multiband system, which is consistent with the band structure calculation [13].

C. Critical current density and STEM images

The J_c in $KCa_2Fe_4As_4F_2$ for sample No. 1 was evaluated by measuring the irreversible magnetization. First, in-plane J_c for $H \parallel c$ axis, which we simply call J_c, was evaluated from magnetization measurements. In the conventional method, J_c can be evaluated using the extended Bean model $J_c = 20\Delta M/a(1 - a/3b)$, where ΔM[emu/cm^3] is M_{down}-M_{up}. M_{up} and M_{down} are the magnetization when sweeping the field up and down, respectively, and a [cm] and b [cm] are the sample width and length ($a < b$) [23,46,47]. For some magnetization data, however, ΔM is reduced in the return branch and causes a non-negligible errors in the calculation of J_c. So J_c was calculated from the magnetization of the second quadrant of the magnetic hysteresis loop in Fig. 7(a) using the extended isotropic Bean model, $J_c = 40M_{down}/a(1 - a/3b)$, after subtracting linear background, as described in Ref. [48]. Figure 7(a) shows the magnetic field dependence of magnetization at various temperatures. Evaluated J_c as a function of temperature is summarized in Fig. 7(b). J_c at 2 K under the self-field is 8.2 MA/cm^2. This value of J_c is significantly larger than those of other IBSs in the same condition, such as $Ba(Fe,Co)_2As_2$ (1.0 MA/cm^2) [49], $BaFe_2(As,P)_2$ (1.4 MA/cm^2) [50], $(Ba,K)Fe_2As_2$ (2.4 MA/cm^2) [51], and $CaKFe_4As_4$ (1.6 MA/cm^2) [28]. It is noteworthy that this value is larger than $J_c \sim 3$ MA/cm^{-2} of the $YBa_2Cu_3O_7$ single crystal without pinning center, at 4.2 K self-field [52,53]. The value of J_c at 20 K under the self-field is 0.38 MA/cm^2. This value agrees reasonably well with that evaluated from the analysis of the MO image. A slight underestimation of J_c evaluated from the MO image may be caused by the effect of observed defect or a slightly larger gap between the sample surface and the garnet film. J_c decreases monotonically with the magnetic field without showing the peak effect in the whole temperature range. At temperatures above 20 K, the magnetic field dependence of J_c becomes remarkable as shown in Fig. 7(b). This is consistent with the low irreversibility field near T_c as described in Fig. 4(c). Next,

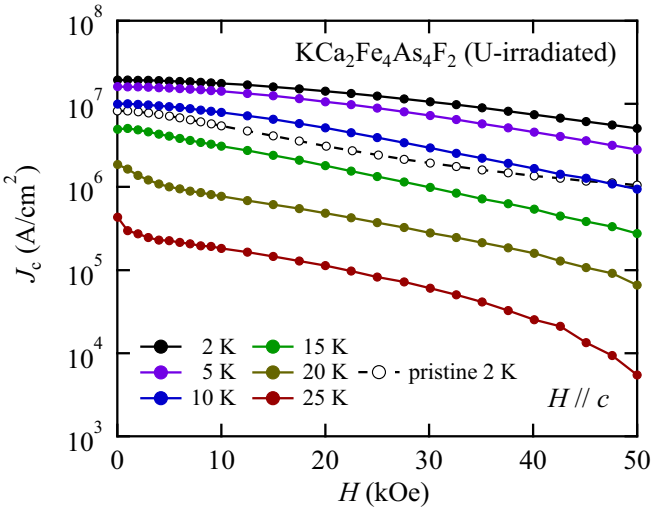

FIG. 8. Magnetic field dependence of magnetic J_c at various temperature in 2.6 GeV U-irradiated ($B_\Phi = 40$ kOe) $KCa_2Fe_4As_4F_2$. Open circles with a dashed line show the data of the pristine sample at 2 K shown in Fig. 7(b) for comparison.

we demonstrate further enhancement of J_c by swift-particle irradiation. It is well known that point or columnar defects created by swift-particle irradiation work as pinning centers for vortices and increase J_c [49]. We introduced columnar defects by using 2.6 GeV U-ion irradiation at a dose equivalent field of $B_\Phi = 40$ kG. The J_c as a function of magnetic field of the $KCa_2Fe_4As_4F_2$ is summarized in Fig. 8. The J_c in 2.6 GeV U-ion irradiated sample No. 7 was calculated by the same method for that in the pristine sample. After the irradiation, J_c at 2 K under the self-field is enhanced up to $\sim$19 MA/cm^2, which is more than twice the value of the pristine crystal. The largest value of J_c obtained at 2 K under self-field in 2.6 GeV U-irradiated $KCa_2Fe_4As_4F_2$ is slightly larger than those in heavy ion-irradiated $(Ba,K)Fe_2As_2$, $\sim$15 MA/cm^2 [54]. J_c can be enhanced by introducing a proper amount of defects as pinning centers with proper energy of particles. For instance, in the case of $(Ba,K)Fe_2As_2$, J_c is enhanced by changing B_Φ, and the optimal B_Φ to achieve the maximum J_c depends on the particles such as Au, U, and Xe, and their energy [54]. Furthermore, when splayed columnar defects are induced to $YBa_2Cu_3O_7$ or $(Ba,K)Fe_2As_2$, J_c can be enhanced even further compared with that for columnar defects parallel to the c axis [52,55]. Considering the similarity between $(Ba, K)Fe_2As_2$ and $KCa_2Fe_4As_4F_2$, J_c in this material is expected to be enhanced by optimizing the irradiation condition. Using flux quantum Φ_0, coherence length ξ, penetration depth λ, and speed of light c, depairing the current density J_d is given by the following formula [56]:

$$J_d = \frac{c\Phi_0}{12\sqrt{3}\pi^2\xi\lambda^2}.$$

Using the $\lambda(T = 0)$ [19,57], and $\xi(T = 0)$, calculated from $H_{c2}^c(0\,\mathrm{K}) = 1326$ kOe as described in the above discussion, $J_d = 121$ MA/cm^2 is estimated. The highest obtained $J_c = 19$ MA/cm^{-2} in the irradiated crystal is $\sim$16% of calculated J_d.

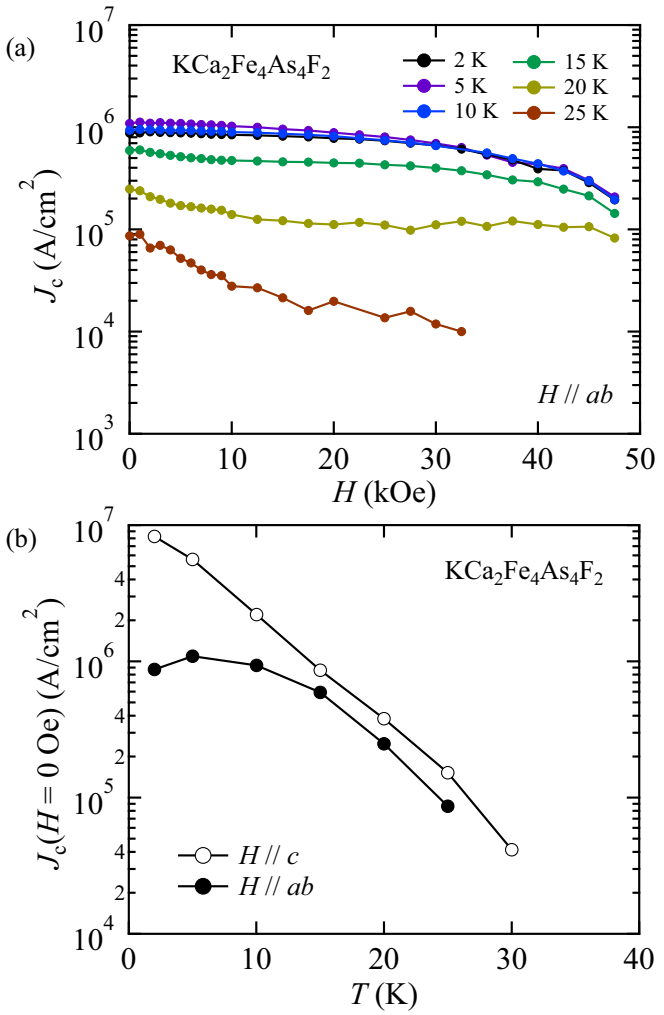

FIG. 9. (a) Magnetic field dependence of magnetic J_c in $KCa_2Fe_4As_4F_2$ at various temperatures for $H \parallel ab$ plane. (b) Temperature dependence of magnetic J_c under the self-field in $KCa_2Fe_4As_4F_2$ for $H \parallel c$ axis and $H \parallel ab$ plane.

In the case of compounds with tetragonal symmetry, three kinds of J_c should be considered. One of them is in-plane J_c when the field is applied along the c axis as discussed above. The others are two independent critical current densities for $H \parallel ab$ plane, one flows in the ab plane and another flows along the c axis. We tentatively designate the former as J_{c2} and the latter as J_{c3} (following the definition in Ref. [28]). However, it is difficult to evaluate J_{c2} and J_{c3} independently without a large difference between J_{c2} and J_{c3} as in the case of $CaKFe_4As_4$ [28]. Hence, we only evaluated average J_c for the $H \parallel ab$ plane, $J_c^{H\parallel ab}$, using the extended Bean model for sample No. 1 as shown in Fig. 9(a). Since the return branch cannot be estimated well due to the small magnetization compared with the background signal, J_c is calculated using the conventional extended Bean model $J_c = 20\Delta M/a(1\text{-}a/3b)$. Figure 9(b) shows the temperature dependence of $J_c^{H\parallel ab}$ under self-field together with the self-field J_c for c axis ($J_c^{H\parallel c}$). The self-field $J_c^{H\parallel ab}$ at 2 K is $\sim$0.9 MA/cm^2. Compared with $J_c^{H\parallel c}$, the value of $J_c^{H\parallel ab}$ is smaller, especially below 10 K. $J_c^{H\parallel c}$ under self-field is $\sim$9 and $\sim$1.5 times larger than $J_c^{H\parallel ab}$ at 2

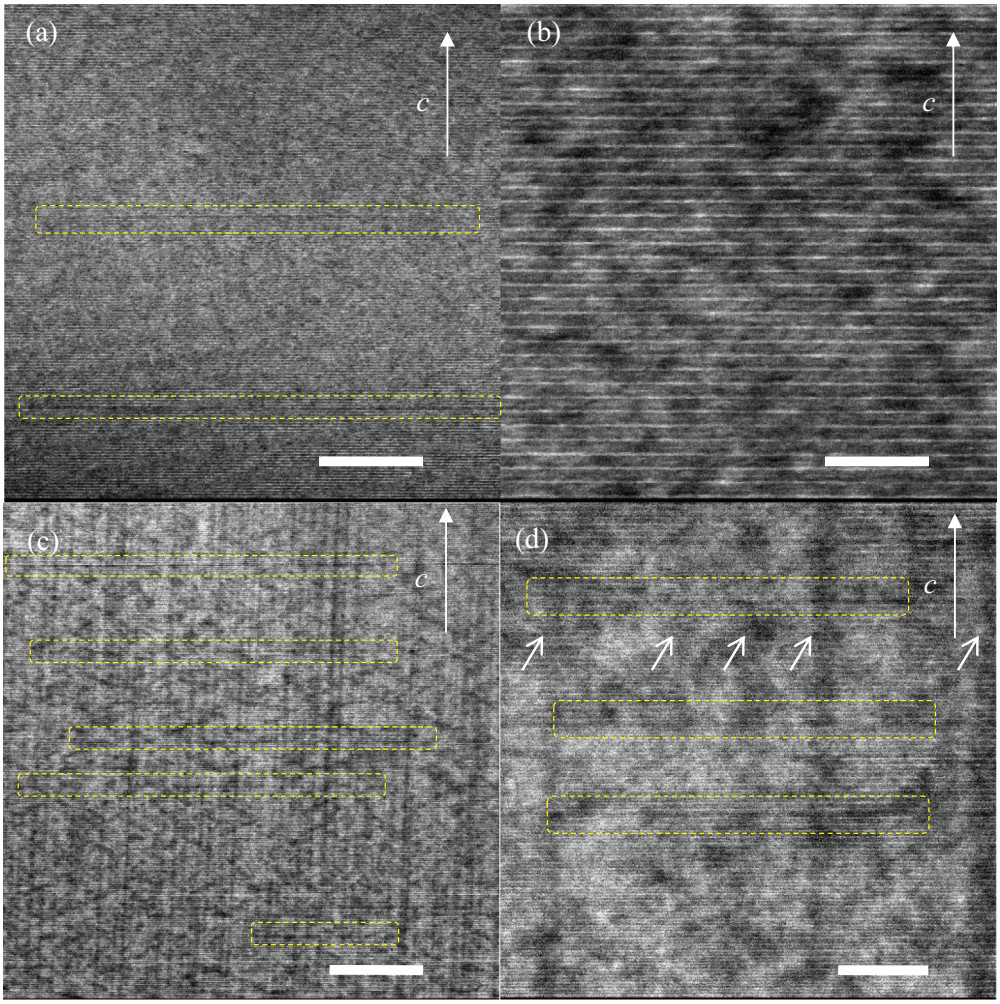

FIG. 10. STEM images of (a), (b) the pristine and (c), (d) 2.6 GeV U-irradiated $KCa_2Fe_4As_4F_2$ for an electron beam injected along the *a* axis. Scale bars in (a)–(d) correspond to 100, 10, 100, and 20 nm, respectively. Yellow dashed squares in (a), (c), (d) emphasize the location of horizontal black lines in STEM images, which we interpret to be thin planar defects. White arrows in (d) emphasize the columnar defects generated by 2.6 GeV U irradiation.

and above 15 K, respectively. While temperature dependence of $J_c^{H\|ab}$ below 10 K is weaker than that of $J_c^{H\|c}$, the values and temperature dependence of $J_c^{H\|c}$ and $J_c^{H\|ab}$ become similar above 15 K. It should be noted that there have been a limited number of studies on the anisotropic J_c and detailed discussion on its origin. So, the mechanism of anisotropic J_c is still not clear. For instance, $Ba(Fe,Co)_2As_2$ and Fe(Te,Se) single crystals are reported to show isotropic J_c [49,58]. On the other hand, $J_c^{H\|ab}$ in $CaKFe_4As_4$ shows the opposite trend ($J_c^{H\|ab} > J_c^{H\|c}$) [59,60], and that in the same 12442-type of $CsCa_2Fe_4As_4F_2$ at 1.8 K shows a similar trend ($J_c^{H\|ab} < J_c^{H\|c}$) [17].

One of the possible reasons for the significantly large and anisotropic J_c could be the presence of natural defects in the pristine $KCa_2Fe_4As_4F_2$. In the case of $CaKFe_4As_4$, where anisotropic J_c was also observed, planar defects nearly parallel to the *ab* plane were detected by STEM observations [28]. If similar defects are present also in $KCa_2Fe_4As_4F_2$, it may be possible to explain anisotropic J_c. Planar defects parallel to *ab* plane work as pinning centers for vortices when magnetic field is applied parallel to the *ab* plane, causing enhancement of J_{c2}, or block electrical current flowing along the *c* axis leading to reduction of J_{c3}. The former effect may be more dominant in $CaKFe_4As_4$. To give a hint for the anisotropic J_c, we performed STEM observations. In STEM images, we observed some black lines parallel to the *ab* plane, which may be due to atomic scale defects, strain, or chemical inhomogeneities. Details of STEM observations and discussion based on the information of observed defects are described in the next paragraph.

Figures 10(a)–10(d) show STEM images on the cross section parallel to the *c* axis in the pristine and 2.6 GeV U-irradiated $KCa_2Fe_4As_4F_2$. The clear periodic structure along the *c* axis in Fig. 10(b) corresponds to a half unit cell of $KCa_2Fe_4As_4F_2$. Horizontal black lines marked by yellow dashed squares are observed in STEM images in Figs. 10(a), 10(c), and 10(d), which we interpret to be thin planar defects. These planar defects extending more than 400 nm are randomly distributed, and the separation between defects is larger than 100 nm. The lower density of defects and longer defects along the *ab* plane in $KCa_2Fe_4As_4F_2$ should reduce J_{c3} effectively rather than increase J_{c2} as opposed to $CaKFe_4As_4$,

leading to the net reduction of $J_c^{H\|ab}$. So the observed defects are possible origin of anisotropic J_c, where $J_c^{H\|ab}$ is lower than $J_c^{H\|c}$, although the detailed structure of defects should be clarified to justify our speculation. On the other hand, no characteristic defect structure along the c axis was observed in the pristine $KCa_2Fe_4As_4F_2$ which may contribute to the increase in $J_c^{H\|c}$. Instead, as shown in Fig. 10(b), regions with dark contrasts with 5–10 nm scale are randomly distributed. Lattice strains or chemical inhomogeneities of some kind can be the cause of these regions with dark contrasts. Higher-resolution STEM observations may shed light on the origin of the atomic scale pinning centers responsible for the very large $J_c^{H\|c}$ in $KCa_2Fe_4As_4F_2$. On the other hand, in 2.6 GeV U-irradiated $KCa_2Fe_4As_4F_2$, clear columnar defects along the c axis are observed as shown in Figs. 10(c) and 10(d), although these defects look a little discontinuous compared with those in 2.6 GeV U-irradiated K-doped $BaFe_2As_2$ [48,61]. A possible reason for this difference is that the threshold energies of the irradiated ions to create the continuous columnar defects are different for each material. Actually, it has been confirmed that the continuity and radius of columnar defects are quite different between $Ba(Fe,Co)_2As_2$ and $(Ba,K)Fe_2As_2$ irradiated by the same 2.6 GeV U ions [61]. The observed columnar defects should work as a pinning center for vortices to increase in plane J_c as shown in Fig. 8. It should be noted that J_c of the irradiated crystal in a higher temperature and magnetic field range shown in Fig. 8 is remarkably larger than that of the pristine crystal shown in Fig. 7(b). This indicates that the irreversibility field above 20 K is enhanced by pinning of vortices introduced by the columnar defect. The higher performance of J_c around 20 K by increasing the pinning force is more advantageous for the operation of those using He-free refrigeration systems in future [2]. Moreover, further enhancement of J_c of $KCa_2Fe_4As_4F_2$ in a wide temperature range is expected. In the case of $Ba_{0.6}K_{0.4}Fe_2As_2$, the degree of enhancement of J_c by heavy-ion irradiation is controlled not only by the matching field, but also by the energy and species of ions [54]. Further enhancement of J_c by exploring the optimal irradiation condition is demanded in the future.

IV. CONCLUSION

We have presented a systematic study of anisotropic physical properties and critical current density in $KCa_2Fe_4As_4F_2$. The sharp onset of diamagnetic shielding and the magneto-optical image reveal the homogeneity of single crystal and prominent Bean-like penetrations of vortices. The temperature dependence of ρ_{ab} shows a tendency of saturation at high temperatures with a value $\sim$300 $\mu\Omega$ cm at room temperature. This is comparable to values of $Ba_{0.5}K_{0.5}Fe_2As_2$ and $CaKFe_4As_4$ with similar doping levels, and is consistent to the universality of the MIR limit in metals. A large anisotropy of electrical resistivity with $\rho_c/\rho_{ab} \sim 100$ at room temperature and semiconductorlike ρ_c suggest quasi-two-dimensional electronic state. R_H analysis indicates that $KCa_2Fe_4As_4F_2$ is a multiband system and holes are dominant carriers. The estimated J_c from the irreversible magnetization at 2 K under the self-field is 8.2 MA/cm^2. This value of J_c is the largest among those of other iron-based superconductors in the same condition, and the large anisotropy of J_c depending on the direction of magnetic field. We found sparsely distributed planar defects and scattered dark contrasts as observed in STEM images. Further enhancement of J_c up to 19 MA/cm^2 at 2 K under self-field is also demonstrated by irradiating 2.6 GeV U at $B_\Phi = 40$ kG. Remarkably large enhancement of J_c is sustained even at high temperatures and high fields.

ACKNOWLEDGMENT

This work was partially supported by a Grant in Aid for Scientific Research (A) (17H01141) from the Japan Society for the Promotion of Science (JSPS).

[1] Y. Kamihara, T. Watanabe, M. Hirano, and H. Hosono, J. Am. Chem. Soc. **130**, 3296 (2008).
[2] H. Hosono, A. Yamamoto, H. Hiramatsu, and Y. Ma, Mater. Today **21**, 278 (2018).
[3] H. Huang, C. Yao, C. Dong, X. Zhang, D. Wang, Z. Cheng, J. Li, S. Awaji, H. Wen, and Y. Ma, Supercond. Sci. Technol. **31**, 015017 (2018).
[4] S. Pyon, D. Miyawaki, T. Tamegai, S. Awaji, H. Kito, S. Ishida, and Y. Yoshida, Supercond. Sci. Technol. **33**, 065001 (2020).
[5] M. Rotter, M. Tegel, and D. Johrendt, Phys. Rev. Lett. **101**, 107006 (2008).
[6] Z-C. Wang, C-Y. He, S-Q. Wu, Z-T. Tang, Y. Liu, A. Ablimit, C-M. Feng, and G-H. Cao, J. Am. Chem. Soc. **138**, 7856 (2016).
[7] Z. Wang, C. He, Z. Tang, S. Wu, and G. Cao, Sci. China Mater. **60**, 83 (2017).
[8] Z.-C. Wang, C.-Y. He, S.-Q. Wu, Z.-T. Tang, Y. Liu, A. Ablimit, Q. Tao, C.-M. Feng, Z.-A. Xu, and G.-H. Cao, J. Phys.: Condens. Matter **29**, 11LT01 (2017).
[9] Z.-C. Wang, C.-Y. He, S.-Q. Wu, Z.-T. Tang, Y. Liu, and G.-H. Cao, Chem. Mater. **29**, 1805 (2017).
[10] S.-Q. Wu, Z.-C. Wang, C.-Y. He, Z.-T. Tang, Y. Liu, and G.-H. Cao, Phys. Rev. Mater. **1**, 044804 (2017).
[11] X. Dong, K. Jin, D. Yuan, H. Zhou, J. Yuan, Y. Huang, W. Hua, J. Sun, P. Zheng, W. Hu, Y. Mao, M. Ma, G. Zhang, F. Zhou, and Z. Zhao, Phys. Rev. B **92**, 064515 (2015).
[12] S. Sun, S. Wang, R. Yu, and H. Lei, Phys. Rev. B **96**, 064512 (2017).
[13] G. Wang, Z. Wang, and X. Shi, EPL **116**, 37003 (2016).
[14] J. Ishida, S. Iimura, and H. Hosono, Phys. Rev. B **96**, 174522 (2017).
[15] B. Wang, Z.-C. Wang, K. Ishigaki, K. Matsubayashi, T. Eto, J. Sun, J.-G. Cheng, G.-H. Cao, and Y. Uwatoko, Phys. Rev. B **99**, 014501 (2019).
[16] M. Smidman, F. K. K. Kirschner, D. T. Adroja, A. D. Hillier, F. Lang, Z. C. Wang, G. H. Cao, and S. J. Blundell, Phys. Rev. B **97**, 060509(R) (2018).

[17] T. Wang, J. Chu, H. Jin, J. Feng, L. Wang, Y. Song, C. Zhang, X. Xu, W. Li, Z. Li, T. Hu, D. Jiang, W. Peng, X. Liu, and G. Mu, J. Phys. Chem. C **123**, 13925 (2019).

[18] Z.-C. Wang, Y. Liu, S.-Q. Wu, Y.-T. Shao, Z. Ren, and G.-H. Cao, Phys. Rev. B **99**, 144501 (2019).

[19] A. B. Yu, T. Wang, Y. F. Wu, Z. Huang, H. Xiao, G. Mu, and T. Hu, Phys. Rev. B **100**, 144505 (2019).

[20] W. Hong, L. Song, B. Liu, Z. Li, Z. Zeng, Y. Li, D. Wu, Q. Sui, T. Xie, S. Danilkin, H. Ghosh, A. Ghosh, J. Hu, L. Zhao, X. Zhou, X. Qiu, S. Li, and H. Luo, Phys. Rev. Lett. **125**, 117002 (2020).

[21] H. Q. Yuan, J. Singleton, F. F. Balakirev, S. A. Baily, G. F. Chen, J. L. Luo, and N. L. Wang, Nature (London) **457**, 565 (2009).

[22] M. M. Altarawneh, K. Collar, C. H. Mielke, N. Ni, S. L. Bud'ko, and P. C. Canfield, Phys. Rev. B **78**, 220505(R) (2008).

[23] Y. Nakajima, Y. Tsuchiya, T. Taen, T. Tamegai, S. Okayasu, and M. Sasase, Phys. Rev. B **80**, 012510 (2009).

[24] D. C. Larbalestier, J. Jiang, U. P. Trociewitz, F. Kametani, C. Scheuerlein, M. Dalban-Canassy, M. Matras, P. Chen, N. C. Craig, P. J. Lee, and E. E. Hellstrom, Nat. Mater. **13**, 375 (2014).

[25] Y. Sun, Y. Tsuchiya, S. Pyon, T. Tamegai, C. Zhang, T. Ozaki, and Q. Li, Supercond. Sci. Technol. **28**, 015010 (2015).

[26] M. Nakajima, S. Ishida, T. Tanaka, K. Kihou, Y. Tomioka, T. Saito, C. H. Lee, H. Fukazawa, Y. Kohori, T. Kakeshita, A. Iyo, T. Ito, H. Eisaki, and S. Uchida, Sci. Rep. **4**, 5873 (2014).

[27] W. R. Meier, T. Kong, U. S. Kaluarachchi, V. Taufour, N. H. Jo, G. Drachuck, A. E. B¨ohmer, S. M. Saunders, A. Sapkota, A. Kreyssig, M. A. Tanatar, R. Prozorov, A. I. Goldman, Fedor F. Balakirev, Alex Gurevich, S. L. Bud'ko, and P. C. Canfield, Phys. Rev. B **94**, 064501 (2016).

[28] S. Pyon, A. Takahashi, I. Veshchunov, T. Tamegai, S. Ishida, A. Iyo, H. Eisaki, M. Imai, H. Abe, T. Terashima, and A. Ichinose, Phys. Rev. B **99**, 104506 (2019).

[29] A. F. Ioffe and A. R. Regel, Prog. Semicond. **4**, 237 (1960).

[30] N. E. Hussey, K. Takenaka, and H. Takagi, Philos. Mag. **84**, 2847 (2004).

[31] Y. Liu, M. A. Tanatar, W. E. Straszheim, B. Jensen, K. W. Dennis, R. W. McCallum, V. G. Kogan, R. Prozorov, and T. A. Lograsso, Phys. Rev. B **89**, 134504 (2014).

[32] N. R. Werthamer, E. Helfand, and P. C. Hohenberg, Phys. Rev. **147**, 295 (1966).

[33] Y. Jia, P. Cheng, L. Fang, H. Luo, H. Yang, C. Ren, L. Shan, C. Gu, and H.-H. Wen, Appl. Phys. Lett. **93**, 032503 (2008).

[34] Z.-S. Wang, H.-Q Luo, C. Ren, and H.-H. Wen, Phys. Rev. B **78**, 140501(R) (2008).

[35] X. F. Wang, T. Wu, G. Wu, H. Chen, Y. L. Xie, J. J. Ying, Y. J. Yan, R. H. Liu, and X. H. Chen, Phys. Rev. Lett. **102**, 117005 (2009).

[36] M. A. Tanatar, N. Ni, G. D. Samolyuk, S. L. Bud'ko, P. C. Canfield, and R. Prozorov, Phys. Rev. B **79**, 134528 (2009).

[37] M. A. Tanatar, M. S. Torikachvili, A. Thaler, S. L. Bud'ko, P. C. Canfield, and R. Prozorov, Phys. Rev. B **90**, 104518 (2014).

[38] Y. Nakamura and S. Uchida, Phys. Rev. B **47**, 8369(R) (1993).

[39] K. Takenaka, K. Mizuhashi, H. Takagi, and S. Uchida, Phys. Rev. B **50**, 6534(R) (1994).

[40] T. Watanabe, T. Fujii, and A. Matsuda, Phys. Rev. Lett. **79**, 2113 (1997).

[41] M. A. Tanatar, N. Ni, A. Thaler, S. L. Bud'ko, P. C. Canfield, and R. Prozorov, Phys. Rev. B **82**, 134528 (2010).

[42] M. A. Tanatar, N. Ni, A. Thaler, S. L. Bud'ko, P. C. Canfield, and R. Prozorov, Phys. Rev. B **84**, 014519 (2011).

[43] M. A. Tanatar, E. C. Blomberg, H. Kim, K. Cho, W. E. Straszheim, B. Shen, H.-H. Wen, and R. Prozorov, arXiv:1106.0533 (2011).

[44] Y. Nakajima, T. Taen, and T. Tamegai, J. Phys. Soc. Jpn. **78**, 023702 (2009).

[45] K. Ohgushi and Y. Kiuchi, Phys. Rev. B **85**, 064522 (2012).

[46] C. P. Bean, Rev. Mod. Phys. **36**, 31 (1964).

[47] E. M. Gyorgy, R. B. van Dover, K. A. Jackson, L. F. Schneemeyer, and J. V. Waszczak, Appl. Phys. Lett. **55**, 283 (1989).

[48] A. Park, S. Pyon, K. Ohara, N. Ito, T. Tamegai, T. Kambara, A. Yoshida, and A. Ichinose, Phys. Rev. B **97**, 064516 (2018).

[49] T. Tamegai, T. Taen, H. Yagyuda, Y. Tsuchiya, S. Mohan, T. Taniguchi, Y. Nakajima, S. Okayasu, M. Sasase, H. Kitamura, T. Murakami, T. Kambara, and Y. Kanai, Supercond. Sci. Technol. **25**, 084008 (2012).

[50] A. Park, I. Veshchunov, A. Mine, S. Pyon, T. Tamegai, and H. Kitamura, Phys. Rev. B **101**, 224507 (2020).

[51] T. Taen, F. Ohtake, S. Pyon, T. Tamegai, and H. Kitamura, Supercond. Sci. Technol. **28**, 085003 (2015).

[52] L. Krusin-Elbaum, A. D. Marwick, R. Wheeler, C. Feild, V. M. Vinokur, G. K. Leaf, and M. Palumbo, Phys. Rev. Lett. **76**, 2563 (1996).

[53] T. Tamegai, L. Krusin-Elbaum, L. Civale, P. Santhanam, M. J. Brady, W. T. Masselink, F. Holtzberg, and C. Feild, Phys. Rev. B **45**, 8201(R) (1992).

[54] F. Ohtake, T. Taen, S. Pyon, T. Tamegai, S. Okayasu, T. Kambara, and H. Kitamura, Physica C **518**, 47 (2015).

[55] A. Takahashi, S. Pyon, T. Kambara, A. Yoshida, and T. Tamegai, J. Phys. Soc. Jpn. **89**, 094705 (2020).

[56] M. Tinkham, *Introduction to Superconductivity*, 2nd ed. (McGraw Hill, New York, 1996).

[57] A. Bhattacharyya, D. T. Adroja, M. Smidman, and V. K. Anand, Sci. China-Phys. Mech. Astron. **61**, 127402 (2018).

[58] Y. Sun, T. Taen, Y. Tsuchiya, Q. Ding, S. Pyon, Z. Shi, and T. Tamegai, Appl. Phys. Express **6**, 043101 (2013).

[59] S. J. Singh, M. Bristow, W. R. Meier, P. Taylor, S. J. Blundell, P. C. Canfield, and A. I. Coldea, Phys. Rev. Mater. **2**, 074802 (2018).

[60] S. Ishida, A. Iyo, H. Ogino, H. Eisaki, N. Takeshita, K. Kawashima, K. Yanagisawa, Y. Kobayashi, K. Kimoto, H. Abe, M. Imai, J. Shimoyama, and M. Eisterer, npj Quant. Mater. **4**, 27 (2019).

[61] N. Ito, S. Pyon, T. Kambara, A. Yoshida, S. Okayasu, A. Ichinose, and T. Tamegai, J. Phys.: Conf. Series **1054**, 012020 (2018).